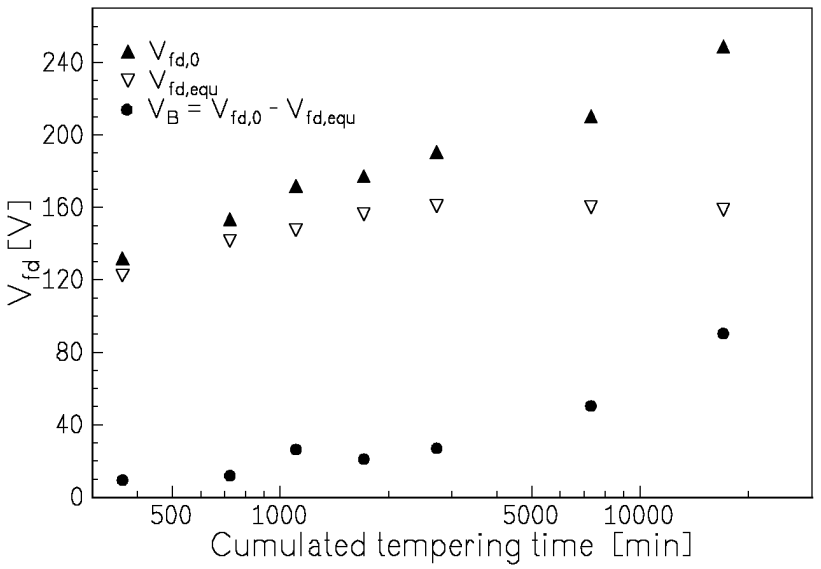

Figure 6.18: Depletion voltage versus cumulated tempering time, T = 80°C, (941G02)

constant $\tau_B = 400 \pm 60$min. But this behaviour can be observed only after sufficient heat treatment. The depletion voltage of a sample stored at room temperature for 3 years could not be changed by forward current ($\Phi = 2{\cdot}10^{13}$ n cm^{-2} , 911K35). Hence, it seems to be likely to assume a bistable defect to be generated by the heat treatment which can be switched between its electrically active and non-active states (see fig. 6.19). Since current injection and illumination are activating the defect, it is important to avoid strictly forward current measurements and light on the sample before making measurements on the reverse annealing.

In order to determine the fluence dependence of N_B its increase normalised to

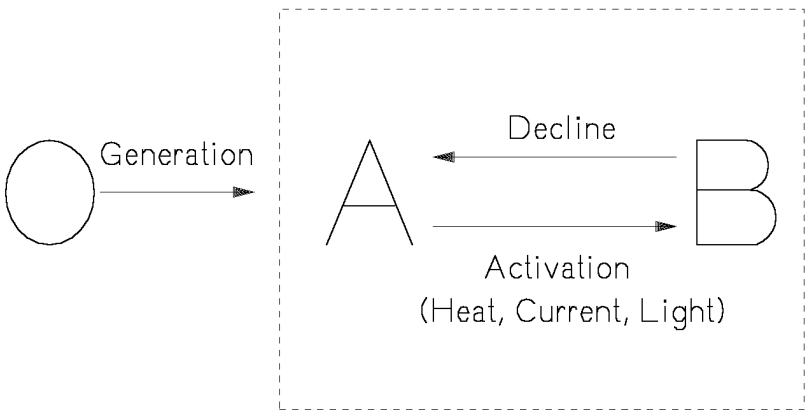

Figure 6.19: Schematic of the bistable defect.

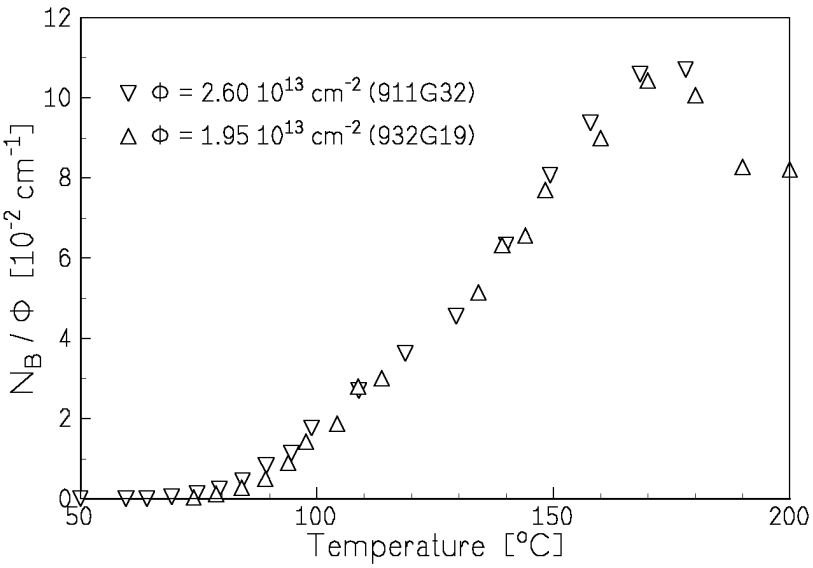

Figure 6.20: Increase of N_B normalised to fluence during isochronal heat treatments.

fluence during an isochronal heat treatment is plotted in fig. 6.20. It can be seen that at 180°C N_B/Φ reaches the maximum value 0.11 cm^{-1}. Above 180°C N_B decreases again. Although the fluences of both samples used for the isochronal heat treatments differ by a factor of two, N_B/Φ has the same value during the total treatment suggesting N_B grows in proportion to Φ.

The data obtained from the isothermal heat treatments are summarised in tab. 6.6. From the tempering experiments at different temperatures with different cumulated tempering times the following conclusion can be made :

- No significant concentration of the bistable defect is generated at room temperature within 37 months in an irradiated sample (911K35) and no effect could be found in a non-irradiated sample (936G26).
- No generation can be seen in not-inverted material. Although both samples, 941G01 (not-inverted after irradiation) and 941G02 (inverted after irradiation) were tempered at 80°C for the same time, the N_B/Φ value of the not-inverted sample is much smaller and no bistable behaviour has been seen before it has been driven to type inversion by the heat treatment. A possible explanation is that the generation of the bistable defect does not start before the type inversion, and thus the time of generation is shorter for the sample 941G01.
- The bistable defect is also generated in p-type material (936G19).

6.1.3 Short Term Annealing

In order to find a parametrisation of the short term annealing it is necessary to subtract all long term components. These components and their behaviour in time

Φ $[cm^{-2}]$ 10^{11}	T [°C]	Time	N_B $[cm^{-3}]$ 10^{11}	N_B/Φ $[cm^{-1}]$ 10^{-2}	Sample
0	120	180 min	0.0	0.0	936G26
200	21	37 mths	0.0	0.0	911K35
41.3	80	5 d	0.0	0.0	941G01
	80	12 d	0.12	0.28	
	80	23 d	0.24	0.59	
219	80	5 d	4.21	1.92	941G02
	80	12 d	7.55	3.45	
198	80	12 d	6.93	3.50	941G37
119	82	5679 min	3.86	3.2	937G04
	120	30 min	4.4	3.7	
147	78	3216 min	2.7	1.8	937G02
312	50	50 d	4.4	1.4	936G19
316	50	57 d	4.0	1.4	935G19
334	77	645 min	3.1	0.9	MUEA13

Table 6.6: Individual results of investigation on the bistable defect.

are very well known from the analysis of the reverse annealing. Since the parameters, such as $N_{Y,\infty}$ and N_C differ slightly from sample to sample each set of data $\Delta N_{eff}(t)$ has been corrected with the parameters as found from individual analysis.

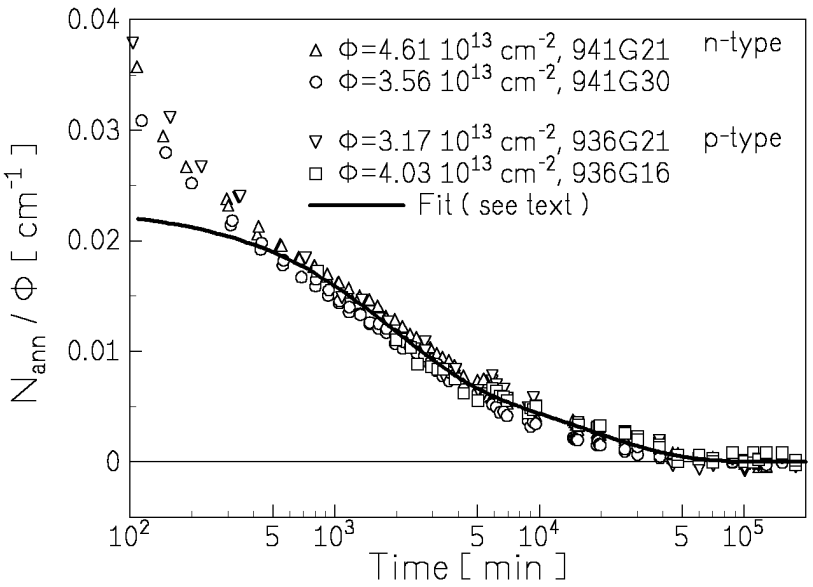

Figure 6.21: Short term annealing of n- type (941) and p-type (936) samples irradiated with high fluences.

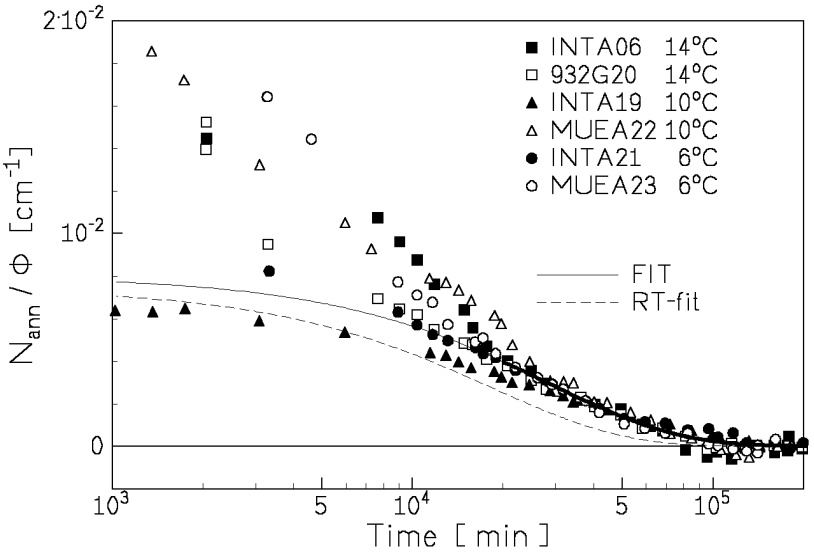

Figure 6.22: Short term annealing at lower temperatures.

After subtraction one gets the concentration of all annealing defects N_{ann} :

$$N_{ann}(t) = \Delta N_{eff}(t) - N_C - N_Y(t). \tag{6.17}$$

$\Delta N_{eff}(t)$ has been defined in eq. 6.2, $N_Y(t)$ is given in eq. 6.9.

The room temperature annealing behaviour of n-type and p-type samples is the same after irradiation with high fluences ($\Phi > \Phi_{inv}$). The data shown in fig. 6.21 were fitted to a sum of two exponential functions :

$$N_{ann}(t) = b_I * \exp(-t/\tau_I) + b_{II} * \exp(-t/\tau_{II}) \tag{6.18}$$

and the following results were obtained :

$$\begin{array}{rclrcl} \tau_I & = & 1.80{\cdot}10^3 \text{ min}, & b_I & = & 1.5{\cdot}10^{-2} \text{ cm}^{-1} \text{ and} \\ \tau_{II} & = & 1.84{\cdot}10^4 \text{ min}, & b_{II} & = & 7.5{\cdot}10^{-3} \text{ cm}^{-1}, \end{array}$$

The error in time constants is about 10%, and for the amplitudes the error is smaller than 6%. The very short time range ($t < 500$ min) has been neglected, because it was comparable to the time of exposure.

The short term annealing at lower temperatures is shown in fig. 6.22. [4] It can be seen that in the time range below $2{\cdot}10^4$ min the data vary strongly. Neither a temperature dependence which could be expected is evident nor the different fabrication processes of the samples seem to influence the result.

Above $2{\cdot}10^4$ min the annealing of all samples can be fitted by the same time constant :

$$\tau_{cold} = 2.9\ (\pm\ 0.1)\ {\cdot}10^4 \text{ min}.$$

[4] Annealing curves of samples 937G30, 932G04 and MUEA24 (one of each set) are not shown and were not fitted, because they deviate in a non-systematic way.

The amplitude is found to be $b_{cold} = 8.0\ (\pm\ 0.4)\ \cdot 10^{-3}$ and agrees very well with value obtained for b_{II}. As for the very short time range the expected temperature dependence, namely an increase of the time constant with lower temperature, can not be found. For comparison also the long time constant annealing from the room temperature annealing is shown in fig. 6.22.

6.1.4 Effective Doping Concentration at Lower Temperature

The annealing behaviour of the effective doping concentration at lower temperature has been investigated assuming the effective doping concentration itself to be independent of the temperature. It will be shown in the following that this assumption holds true, because the temperature dependence in the range under investigation is negligible.

However, a considerable change of the effective space charge has been found for temperatures below 200 K. CV-characteristics of an unirradiated and an irradiated sample measured in a temperature range between 80 K and room temperature are compared in fig. 6.23. It can be seen clearly that the depletion voltage of the unirradiated sample does not change in the entire temperature range, while the depletion voltage of the irradiated sample shifts from about 70 V at room temperature to below 50 V at 80 K. Fig. 6.24 demonstrates that after low fluence irradiation the change of V_{fd} due to temperature is independent of the frequency, while after high fluence irradiation ($\Phi > 4.0{\cdot}10^{12}$ cm^{-2}) a certain frequency dependence becomes visible. No data below 230 K are shown in the right part of the figure, because the CV-characteristics become flat, i.e. already at low voltages the geometrical capacitance is reached. Hence V_{fd} can not be extracted and the investigation of V_{fd}(T) is limited to a low fluence region.

According to eq. 2.26 a decrease in V_{fd} corresponds to a decrease in N_{eff}. The change of N_{eff} with respect to its value at room temperature ($N_{eff}(RT) - N_{eff}(T)$) is shown in fig. 6.25. It can be seen that the difference grows only slowly with falling temperature down to about 180 K. Between 180 K and 140 K a severe drop occurs and below 140 K again only a small decrease can be observed. For comparison also values of N_{eff} are shown which were obtained by determining the slope (see eq. 4.4) of 1 MHz CV-measurements.[5] No difference in the temperature dependence can be seen. The behaviour of the values obtained from the p-type sample is less pronounced, but similar. A section of the difference $N_{eff}(RT) - N_{eff}(T)$ at $T = 103$ K is plotted versus fluence in fig. 6.26. The values obtained from the n-type samples can be fitted by a straight line:

$$N_{eff}(RT) - N_{eff}(103K) = 1.39\ \text{cm}^{-1} \cdot \Phi + 4.1{\cdot}10^{10}\ \text{cm}^{-3},$$

but not the result from the p-type sample. The above given fluence dependence is just a parametrisation and still lacks physical interpretation.

The change of the effective space charge is at least partly a consequence of deep levels which gain influence at lower temperature, because the emission rates become comparable with the duration of a CV-measurement ($\approx$ 10 min). For example [6], the

[5] performed in conjunction with DLTS-measurements.

[6] from the DLTS-results

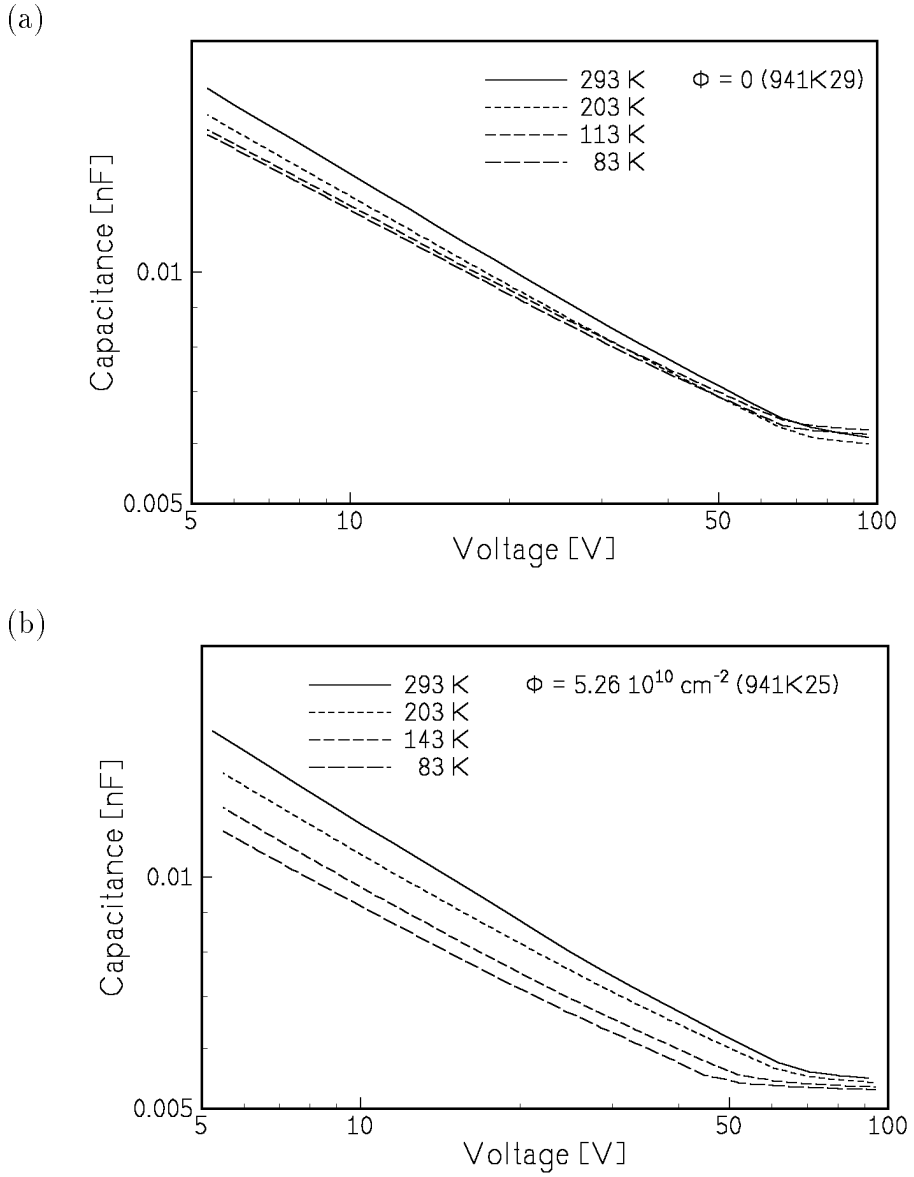

Figure 6.23: CV-measurements (10 kHz) at different temperatures. (a) : before irradiation, (b) : after irradiation.

emission rate of a trap with $\Delta E_T = 0.42$ eV and $\sigma = 2{\cdot}10^{-15}$ cm^2 at 150 K is about 10^3 s^{-1} corresponding to a time constant $\tau = 17$ min. Thus most of the traps do not emit their electron during the measurement. Furthermore the depletion voltage depends also on the duration of a measurement. This effect has been observed, but it needs further investigation.

The temperature dependence of the effective space charge affects considerably the determination of the trap concentration by DLTS. Because the evaluation of n_T requires precise knowledge of N_{eff} (see eqs. 4.21 and 4.53), it is necessary to apply the actual value N_{eff}(T) instead of the room temperature value.

However, for the investigation of the long term annealing behaviour of the ef-

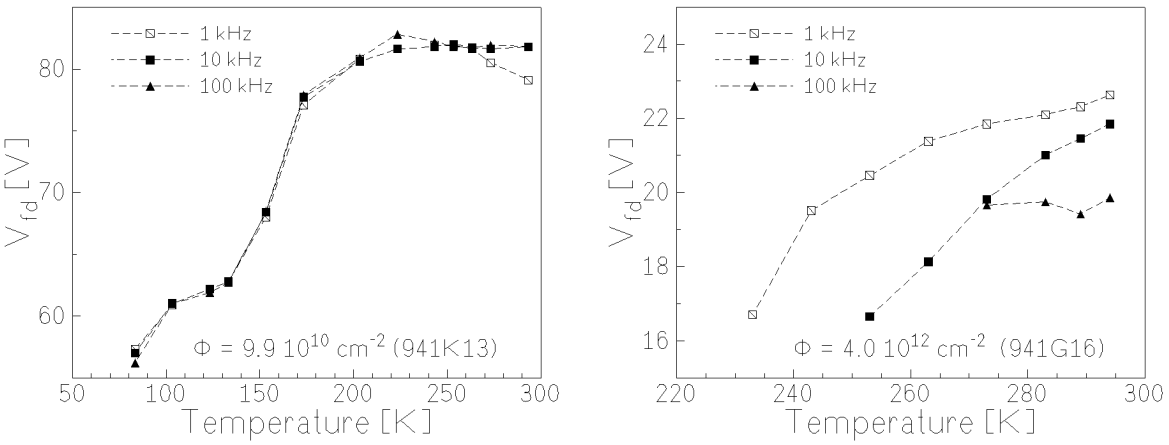

Figure 6.24: Frequency dependence of depletion voltage at various temperatures. Data shown in the right figure are obtained from the measurements already shown in fig. 4.2.

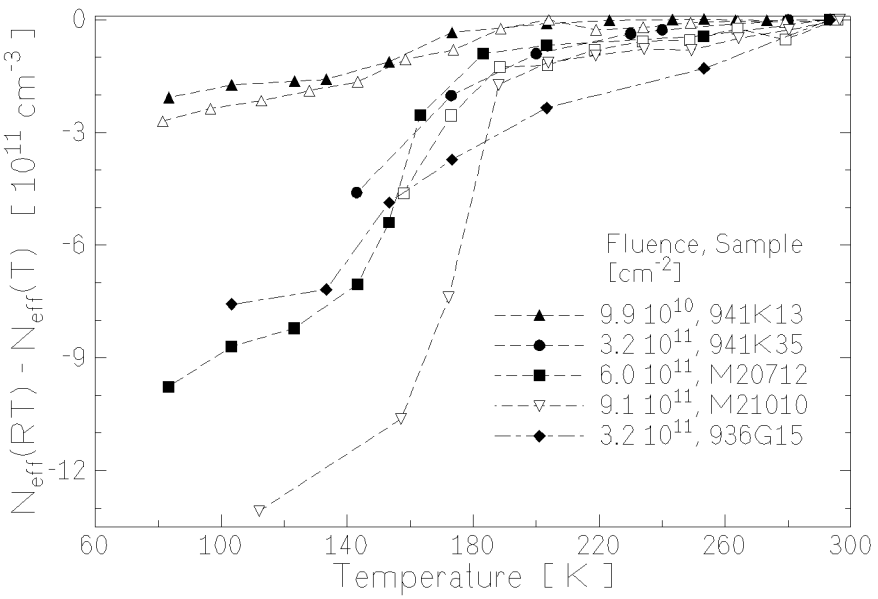

Figure 6.25: Change of effective space charge versus temperature. Filled symbols represent values obtained from the depletion voltage (10 kHz CV-measurements), empty symbols represent values obtained from the slope of 1 MHz CV-measurement.

fective doping concentration at temperatures between 0°C and room temperature the temperature dependence of V_{fd} can also be neglected for samples irradiated with fluences above $4{\cdot}10^{12}$ cm^{-2} because it is always smaller than the error in the analysis of the CV-measurement. E.g. the depletion voltages of a sample (941G23) exposed to $2{\cdot}10^{13}$ cm^{-2} measured at 0°C and 20°C differ by only 1.6 V, while the error is about ± 2 V.

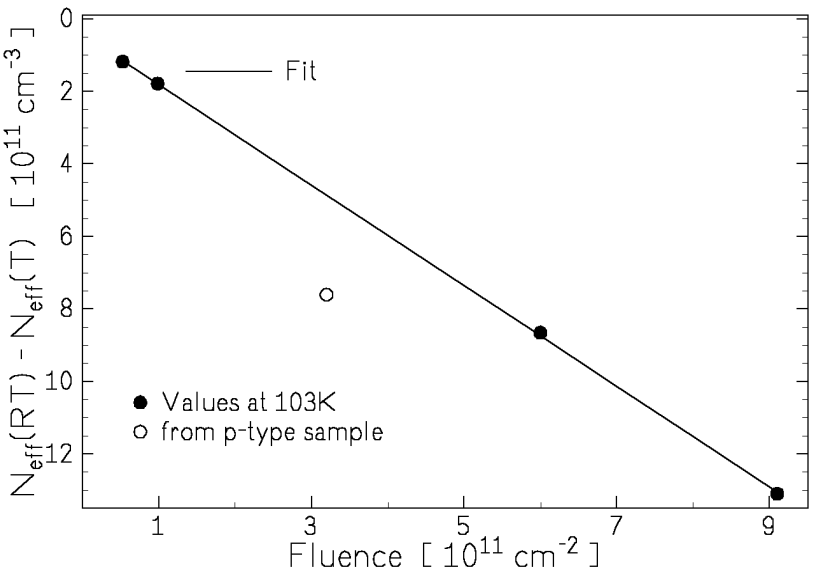

Figure 6.26: Change of effective space charge versus fluence. Filled symbols represent values obtained from n-type samples, empty symbol represents values obtained from p-type sample. The value corresponding to the highest fluence is extracted from the slope.

6.2 Results on Current

6.2.1 Introduction

The increase of the reverse current with fluence is commonly described by :

$$\Delta J = \alpha \Phi, \tag{6.19}$$

where ΔJ is the difference of current density before and after irradiation, and α the *current damage constant*. The microscopic explanation of a constant ratio $\Delta J/\Phi$ is the production of generation centres in proportion to the fluence.

In order to compare the values of α given in the literature additionally to the self-annealing effects the temperature correction according to eq. 4.6 has to be considered. All data given in this work are normalised to 20°C if not mentioned otherwise. The values of the current damage constant as obtained by different experimenters are summarised in tab. 6.7.

Wunstorf found that the fluence dependence as given in eq. 6.19 is valid only as long as the material is not inverted. If $\Phi > \Phi_{inv}$, which is the fluence needed to invert the material, the increase of current with fluence has to be described by

$$\Delta J = \alpha \Phi + \alpha^*(\Phi - \Phi_{inv}), \tag{6.20}$$

with $\alpha = 8{\cdot}10^{-17}$ A cm^{-1} (compare tab. 6.7) and $\alpha^* = 9.8{\cdot}10^{-17}$ A cm^{-1}. The inversion fluence of the material under investigation was $\Phi_{inv} = 4 \cdot 10^{12}$ cm^{-2}. This result has been obtained by applying different annealing corrections to data of inverted and not inverted material. As for the annealing of the effective impurity

α [10^{-17} A cm^{-1}]	Neutron Source	Neutron Energy [MeV]	Reference
6.7 ± 0.4	CERN PSAIF	≈ 1	[76]
6.0 ± 1	ISIS	≈ 1	[78]
8.0 ± 0.1	PTB	< 5.3 >	[36]

Table 6.7: Damage constant α from different experimenters. All values were normalised to 20°C. Fluences are 1 MeV equivalent.

concentration a sum of exponential functions has been used to describe the current annealing :

$$\frac{\Delta J(t)}{\Delta J(0)} = \sum_{i=1}^{n} A_i \exp\left(\frac{-t}{\tau_i}\right), \tag{6.21}$$

with $n = 6$ in case of not inverted material and $n = 5$ for inverted material. The time constants and amplitudes are listed in tab. 6.8. Both, the fluence dependence

No.	Not Inverted		Inverted	
	Time Constant τ_i [min]	Relative Amplitude A_i	Time Constant τ_i [min]	Relative Amplitude A_i
1	$(1.78 \pm 0.17)10^1$	0.156 ± 0.030	$(1.35 \pm 0.03)10^1$	0.197 ± 0.010
2	$(1.19 \pm 0.03)10^2$	0.116 ± 0.003	$(8.34 \pm 0.02)10^1$	0.300 ± 0.002
3	$(1.09 \pm 0.01)10^3$	0.131 ± 0.002	$(1.55 \pm 0.40)10^3$	0.121 ± 0.002
4	$(1.48 \pm 0.01)10^4$	0.201 ± 0.002	$(8.74 \pm 0.48)10^3$	0.139 ± 0.014
5	$(8.92 \pm 0.59)10^4$	0.093 ± 0.007	∞	0.243 ± 0.003
6	∞	0.303 ± 0.006	-	-

Table 6.8: Annealing parameters of the reverse current according to eq. 6.21 [36]

and the annealing behaviour as found by Wunstorf are shown in fig. 6.27.

In the following sections it will be shown that indeed the annealing behaviour depends on the conduction type. In order to obtain current annealing parameters in a time and fluence range corresponding to those used for parametrisation of the N_{eff}-annealing a new set of annealing parameters has been determined. Furthermore the fluence dependence of the non-annealing fraction of current has been investigated.

6.2.2 Fluence Dependence at Room Temperature

As will be shown in sec. 6.2.3 the annealing of the reverse current reaches a constant value at about $2{\cdot}10^5$ min (≈ 140 days) after the irradiation. No reverse annealing as for the effective doping concentration has been observed at room temperature and thus currents I_{final} measured at times $t > 2{\cdot}10^5$ min can be regarded as final values. In fig. 6.28 these values are plotted versus fluence. Additionally the smallest currents measured during heat treatments (see also sec. 6.2.3) are plotted in the same figure. Since no significant deviation can be seen these minimum values I_{min}

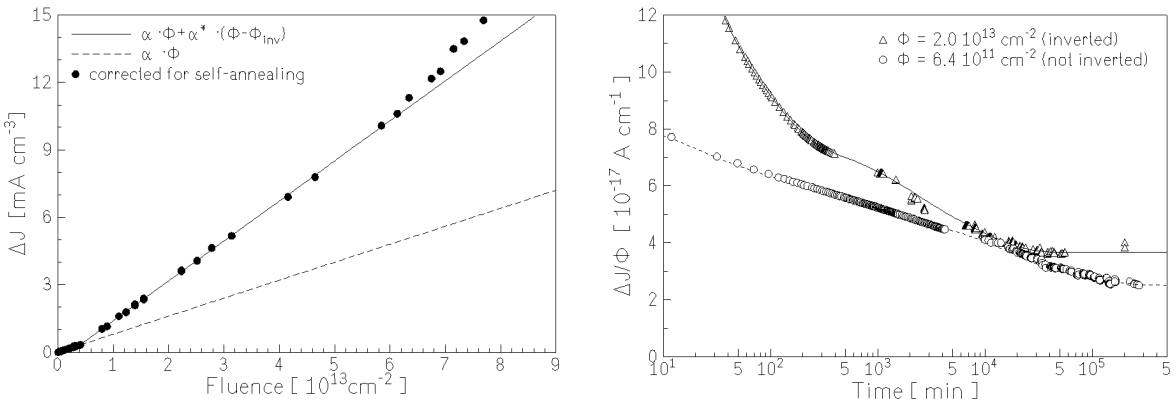

Figure 6.27: Fluence dependence (left) and annealing behaviour of inverted and not inverted material (right) [36].

obviously describe the same annealing state as I_{final}, i.e. the non-annealing fraction of the reverse current I_∞ or the current density J_∞ respectively. Hence both I_{final} and I_{min} have been applied to determine the fluence dependence $\Delta J_\infty(\Phi)$.

First guess to describe the fluence dependence as shown in fig. 6.28 is to use eq. 6.19, because seemingly the current density increases in proportion to the fluence. But from a more detailed view it can be seen that a description according eq. 6.20 matches the data even better. A fit to all data in the fluence range $\Phi > 2 \cdot 10^{13}$ cm^{-2} intersects the Φ-axis at $\Phi \approx 3.6 \cdot 10^{12}$ cm^{-2} . This is a fluence very close to the inversion fluence found by Wunstorf for similar material. Thus the fluence dependence of the non-annealing reverse current is given by :

$$\Delta J_\infty = \alpha_\infty \Phi + \alpha^*_\infty (\Phi - \Phi_{inv}), \tag{6.22}$$

with

$$\begin{aligned} \alpha_\infty &= 1.72\ (\pm\ 0.27) \cdot 10^{-17}\ \text{A cm}^{-1}, \\ \alpha^*_\infty &= 4.86\ (\pm\ 0.02) \cdot 10^{-17}\ \text{A cm}^{-1} \text{ and} \\ \Phi_{inv} &\approx 3.6 \cdot 10^{12}\ \text{cm}^{-2}\ . \end{aligned}$$

The lower part of fig. 6.28 shows how the ratio $\Delta J_\infty/\Phi$ depends on the fluence. For fluences above $3{\cdot}10^{13}$ cm^{-2} the ratio saturates at a certain value as it is expected, because the behaviour as described exactly by eq. 6.22 and the corresponding parameters differs only slightly from a straight line. Thus for practical purposes such as an estimate of the long term development of the reverse current after high fluence exposure it is proposed to make use of the saturation value of the ratio $\Delta J_\infty/\Phi$:

$$\overline{\alpha_\infty} = 4.4\ (\pm\ 0.4) \cdot 10^{-17}\ \text{A cm}^{-1}.$$

Figure 6.28: Top : Fluence dependence of the reverse current density. Parametrisation according to eq. 6.20. See text for values of α_∞. Bottom : Individual values of ratio $\Delta J/\Phi$ versus fluence. The broken line guides the eye.

6.2.3 Time Dependence at Room Temperature and during the Heat Treatments

The reverse current normalised to volume and fluence of various samples as function of time is shown in fig. 6.29. From a certain time on ($t > 2{\cdot}10^3$ min) the annealing curves are rather similar, the only difference is an individual offset. Furthermore it is evident that after $2{\cdot}10^5$ min ($\approx$ 4 months) a constant value is reached which has been introduced as $\Delta J_\infty/\Phi$ in the last section (sec. 6.2.2). This is in contrast to the effective doping concentration which increases significantly even at room temperature after a minimum value has reached at about half a month. This reverse annealing has been described comprehensively in sec. 6.1.2.

Comparing the data and the annealing curve calculated from the annealing parameters given in tab. 6.8 it becomes obvious that the time constants τ_3 and τ_4 are

Figure 6.29: Time dependence of reverse current per volume and fluence. Curves which stop at $3 \cdot 10^4$ min are from samples used for the heat treatments (see sec. 6.1). The fit is calculated according to the parameters for inverted material given in tab. 6.8.

Figure 6.30: Fitted time dependence of current density per fluence. Individual offsets were subtracted. Only those curves were fitted which reached the saturation value. The results of the fit $(\tau_I, \tau_{II}, a_I, a_{II})$ are given in the text.

too short. Hence new time constants were fitted to the data for $t > 2000$ min which is the range of interest for long term prediction. As shown in fig. 6.30 a sum of two exponential functions fits the annealing data very well, if the individual offsets $\Delta J_\infty/\Phi$ are subtracted before. The following time constants and amplitudes were found :

$$\begin{aligned} \tau_I &= 2.65 \cdot 10^3 \text{ min}, \quad a_I = 2.154 \cdot 10^{-17} \text{ A cm}^{-1} \text{ and} \\ \tau_{II} &= 2.30 \cdot 10^4 \text{ min}, \quad a_{II} = 1.840 \cdot 10^{-17} \text{ A cm}^{-1}, \end{aligned}$$

according to :

$$\frac{\Delta J(t)}{\Phi} - \frac{\Delta J_\infty}{\Phi} = a_I * \exp(-t/\tau_I) + a_{II} * \exp(-t/\tau_{II}). \tag{6.23}$$

The error in time constants and amplitudes is about 5%. As expected both time constants are longer than the corresponding numbers given in tab. 6.8. However the ratio of the amplitudes is roughly the same in both cases :
$A_3 : A_4 : A_5 \approx a_I : a_{II} : \Delta J_\infty/\Phi \approx 1 : 1 : 2$.

Figure 6.31: Current annealing during heat treatments.

A less conclusive picture emerges from the annealing behaviour at higher temperatures. In fig. 6.31 annealing curves measured at different temperatures are compared. In some cases in a short time range at the beginning of the heat treatments a decrease of the current can be observed, but finally in all cases the current increases with tempering time. Note, that this applies also for the low irradiated sample (941G01). Apparently the annealing behaviour can not be described in a simple way as fluence dependent or normalised to the volume. Hence, it has to be assumed that the change of current during the heat treatments is not caused by generation centres in the bulk. It is conceivable, that surface and interface properties are affected by the heat treatments which cause the rise of the current.

The annealing parameters as determined by Wunstorf [36] are different for not inverted and inverted material. Hence the annealing behaviour has to depend either on the fluence in a general way or on the conduction type of the material. In the first case the parameters for not inverted material should also match for low irradiated p-type material, otherwise the parameters for the inverted material will give a correct description even in the case of low fluence for p-type. In order to decide experimentally between both possibilities p- and n-type detectors were irradiated with low and high fluences, $3{\cdot}10^{12}$ cm^{-2} and $4{\cdot}10^{13}$ cm^{-2} respectively. Fig. 6.32 shows the subsequent annealing of the reverse current normalised to volume and fluence. The difference of n- and p-type annealing can be seen very clearly in the time range 500 to 5000 min. The curves of both p-type samples and the inverted one coincide after shifting them along the y-axis, i.e. subtracting components of the current that do not change in time. It is evident that the annealing curve of the low irradiated n-type sample will not match the p-type curves whatever is added or subtracted.

Thus, it can be concluded that the conduction type of the material has a significant meaning on the current annealing behaviour.

Figure 6.32: Comparison of current annealing in p- and n-type material.

6.2.4 Annealing at Lower Temperature

The annealing behaviour at lower temperature has been investigated using 3 sets of different samples. Each set consisted of one SB-detector and two p^+-n -detectors from *Micron* and *Intertechnique* which were irradiated and afterwards stored at the same temperature. The temperatures were 6°C, 10°C, and 14°C, respectively (see sec. 5.4).